Variability of the downwelling diffuse attenuation coefficient with consideration of inelastic scattering

Xiaobing Zheng, Tommy Dickey, and Grace Chang

In situ time-series measurements of spectral diffuse downwelling irradiance from the Bermuda Testbed Mooring are presented. Averaged diffuse attenuation coefficients of downwelling irradiance, K_d, and their elastic and inelastic components are investigated at seven wavelengths. At shorter wavelengths (<510 nm), K_d is weakly dependent on the solar zenith angle owing to the prevailing scattering effect and therefore can be considered a quasi-inherent optical property. At longer wavelengths (>510 nm), K_d shows a strong dependence on the solar zenith angle. As depth increases, inelastic scattering plays a greater role for the underwater light field at red wavelengths. © 2002 Optical Society of America

OCIS codes: 010.4450, 290.5860, 120.0280, 010.7340, 030.5620, 120.4640.

1. Introduction

The diffuse attenuation coefficient for downwelling irradiance, K_d (in inverse meters), is one of the most commonly determined optical properties of seawater. It is defined as[1]

$$K_d = -\frac{1}{E_d}\frac{\mathrm{d}E_d}{\mathrm{d}z}, \tag{1}$$

where E_d (watts per square meter) is planar downwelling irradiance and z (in meters) is depth (positive downward from the sea surface). K_d is an indicator of the penetrative component of solar radiation. Approximately 90% of the diffuse reflected light from a water body comes from a surface layer of water of depth $1/K_d$. Thus K_d is an important parameter for remote sensing of ocean color.

Strictly speaking, K_d is not a property of the water itself but rather a descriptor of the underwater light field that varies with depth, solar altitude, and time. Early experimental (e.g., Hojerslev[2] in clear water off Sardinia, Nielsen and Aas[3] in turbid Oslofjorden, and Baker and Smith[4] in San Vicente Reservoir near San Diego) and model results[5,6] indicate that the effect of solar elevation on K_d is relatively small. Within reasonable accuracy, K_d has been considered to be independent of the zenith angle and treated as a quasi-inherent optical property (quasi-IOP). However, more recent experimental results obtained by use of time-series data collected with moored instruments in the upper layer of the Sargasso Sea show significant correlation between K_d and solar altitude, especially at the red wavelengths.[7] Numerical simulations based on radiative transfer equations also show the dependence of K_d on the solar zenith angle.[8,9]

Inelastic scattering effects such as Raman scattering[10] and solar-induced fluorescence have been shown to play important roles in the characterization of K_d, especially at the yellow-green to red wavelengths (or $\lambda > 500$ nm). Stavn[11,12] and Stavn and Weidemann[13] used Monte Carlo simulations to show that Raman scattering contributes significantly to downwelling and upwelling irradiance at wavelengths longer than 500 nm and that the fraction of Raman-scattered photons to total photons increases with depth. Berwald *et al.*[14] used radiative transfer models to show that Raman scattering produces strong vertical gradients in the average cosine and the diffuse attenuation coefficient of irradiance, especially at long wavelengths and for low chlorophyll concentrations. They found no Raman effects for blue wavelengths for simulations that used chlorophyll concentrations in the range of 0.05 to 5 mg m^{-3}, but they did find strong effects in the red.

Past studies of K_d variability were based on theoretical analyses and numerical simulations because few *in situ* measurements of K_d at multiple depths

X. Zheng is with the Department of Remote Sensing, Anhui Institute of Optics and Fine Mechanics, Hefei, China. T. Dickey and G. Chang are with the Ocean Physics Laboratory, University of California, Santa Barbara, 6487 Calle Real Unit A, Goleta, California 93117.

Received 14 June 2002; revised manuscript received 14 June 2002.

0003-6935/02/306477-12$15.00/0

and wavelengths, covering a wide and continuous range of solar incident geometry, were available. Stramska and Frye[7] showed that variation in solar altitude could be important for the variability of K_d according to their mooring-based results. They observed increases of K_d at the red wavelengths by more than 50% at depths of 14–35 m and increases of radiance reflectance by more than 100% with changing solar altitude; both phenomena are attributed to inelastic scattering. The time series of E_d and K_d used by Stramska and Frye were limited to only five and three days, respectively. Hence there is a clear need for more data to permit further studies of the variability of K_d and the role of inelastic scattering in the characterization of K_d. When K_d is determined by ship-based profiling methods, a trade-off exists between rapid profiling speed to maintain a relatively constant solar zenith angle during measurements and longer sampling intervals at each depth to minimize fluctuations caused by wave and wave-focusing effects.[15] Profiling methods cannot be used to cover a wide and continuous zenith angle range. Alternatively, radiometers deployed on a mooring at discrete depths provide a means for monitoring long-term ocean optical properties with high temporal resolution.

The objectives of this paper are to (1) describe recent high-temporal-resolution optical measurements in case I, oligotrophic waters, and to quantify the temporal variability of the spectral diffuse attenuation coefficient, (2) quantify the dependence of the spectral diffuse attenuation coefficient with respect to solar altitude under differing sky conditions (clear and overcast), and (3) evaluate the effects of inelastic scattering on the spectral diffuse attenuation coefficient for different light wavelengths, solar elevations, sky and wind (wave) conditions, and ocean depths by use of observations and radiative transfer simulations conducted with the Hydrolight 4.1 model.[16]

2. Measurements and Data Processing

The Bermuda Testbed Mooring (BTM) has been deployed since June 1994 and provides the oceanographic community with a deep-water platform for scientific studies, *in situ* comparisons for satellite ocean color imagers, and testing of new instrumentation.[17,18] The mooring is located at approximately 31°44′ N, 63°10′ W, approximately 80 km southeast of Bermuda in waters of ~4570-m depth. There have been 16 deployments of three- to six-month duration between June 1994 and the present. More than 1200 individual radiometric measurements were obtained during a period of 100 days during deployment #12 (31 July–5 November 1999). These radiometric measurements provide some of the most comprehensive coverage of zenith angle distributional data to date.

The BTM collects a comprehensive suite of meteorological, physical, bio-optical, and chemical data.[17–19] The instrumentation of primary interest for the present study includes moored optical radiometric systems (MORSs) (Fig. 1). MORSs are used

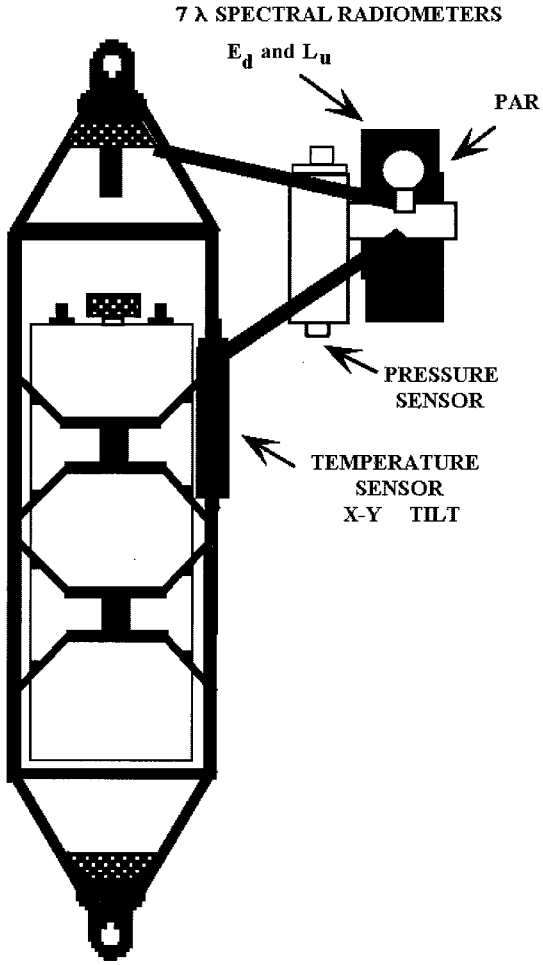

Fig. 1. Schematic diagram of a MORS.

to measure optical properties including spectral downwelling irradiance, E_d, above the surface and at depths of 14 and 21 m along with spectral upwelling radiance, L_u, PAR, temperature, pressure, and tilt at 14- and 21-m depths.

Radiometers (Satlantic, Inc., OCI-200 and OCR-200) are mounted approximately 20 cm off the main frame of the MORS to minimize self-shading effects. The radiometers measure E_d and L_u at seven wavelengths (10-nm full bandwidth at half-maximum) centered at 412, 443, 490, 510, 555, 665, and 683 nm. The radiometers sample once every hour from 6 a.m. to 7 p.m. Bermuda local time at a rate of 6 Hz during a sampling period of 45 s. Data are also sampled at midnight for an evaluation of the background signal.

A. Data Preprocessing

A raw data preprocessing routine was developed to categorize data for analyses. This routine involved (1) computation of solar zenith angles, (2) selection of data sets under different sky conditions, (3) minimization of the random-error factors, and (4) calculation of E_d just below the sea surface. The solar zenith angle at each sampling time was computed with Eqs. (2-2) and (2-3) in Kirk[20]; these computations require

latitude, Julian day, and the sampling time of day. For each sampling time (e.g., 10 a.m. for all deployment days), the corresponding zenith angles were not constant but varied with solar declination. The zenith angles for all deployment days were considered as a whole; therefore they actually covered a quasi-continuous angle range from sunrise to sunset. This is one of the advantageous features of mooring time-series measurements that facilitate the study of the dependence of K_d on illumination geometry.

Cloud cover can significantly affect the angular distribution of skylight and hence the surface and underwater downwelling irradiances. We subdivided our study of K_d variability on the basis of two distinct sky conditions: sunny and overcast. Thus more complex atmospheric effects are avoided. The atmospheric effect on skylight distribution is weaker on sunny days as compared with cloudy days; therefore the irradiance above the sea surface can be determined by the position of the sun in the sky. An approximately cosine-dependent relationship is expected between downwelling irradiance above the sea surface, $E_d(0^+)$, and the solar zenith angle, θ_a, under a sunny sky. Therefore correlation coefficients between $E_d(0^+)$ and cos θ_a at the longest wavelength measured, i.e., 683 nm, at which Rayleigh scattering of the atmosphere is the weakest, were computed at a daily time interval, as shown in Fig. 2(a). By setting an arbitrary threshold for the highest correlation coefficients (value of 0.84) indicated by the dashed line in Fig. 2(a), we chose 40 sunny days from the total 100 deployment days.

To further isolate the best data for our analyses, we then computed the correlation coefficient between $E_d(0^+)$ and $E_d(14$ m) to evaluate the effect of wave focusing, which is one of the main causes of light-field fluctuation in the upper layer of the ocean.[15,21,22] The correlation coefficient between $E_d(14$ m) and $E_d(21$ m) was also calculated to evaluate vertical homogeneity of the water body. Days with the highest product of these two correlation coefficients were selected for detailed analyses among the 40 sunny days, as representatives of data obtained under sunny sky and a calm ocean surface. These 12 daily profiles obtained under sunny sky and calm ocean surface are referred to as the "good" data/days throughout the rest of the paper. Six representative good daily profiles of E_d are shown in Fig. 3(a). Similarly, by setting a threshold for the lowest product of correlation coefficients, 12 "bad" days (representative of cloudy skies and a rough sea surface) were also isolated [Fig. 3(b); six representative daily profiles shown]. Analyses similar to those for the good days were performed for the bad days for comparison.

Large fluctuations of underwater irradiance are observed in our data sets (Fig. 4). The relative deviation of E_d with respect to its mean value can be as large as 70% (Fig. 4). These light fluctuations may be caused by wave action, drifting clouds, and buoy perturbation. Quantitative analyses of these influences on the measurement accuracy of radiometers are given in Appendix A. Intense pulses of radiation

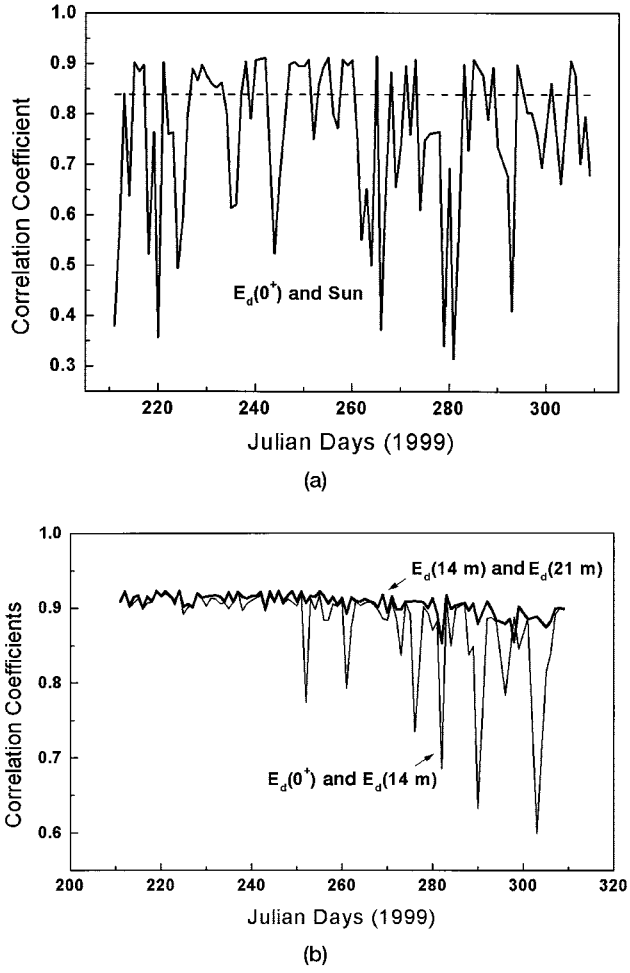

Fig. 2. (a) Correlation coefficient between surface irradiance $E_d(0^+)$ and the cosine of the solar zenith angle. (b) Correlation coefficients between $E_d(0^+)$ and $E_d(14$ m) and between $E_d(14$ m) and $E_d(21$ m).

of duration typically of the order of a few milliseconds can result from the focusing and defocusing of light because of highly energetic waves with periods of 1–30 s.[20] Inspection of our moored radiometric data indicates that the light fluctuates quickly with a typical period of approximately 1–2 s. Therefore averaging over a period of seconds to tens of seconds will be adequate to effectively reduce the error that is due to these short-term variations. A sampling period of 45 s is chosen to minimize the short-term wave effect (periods less than 45 s), as well as to maximize the memory capacity of the radiometers' data loggers. Figure 5 shows the instantaneous and the average diurnal profile of E_d sampled on Julian day 240. Detailed discussions of light-field fluctuation characteristics that are due to the wave effect can be found in Siegel and Dickey,[15] Zaneveld *et al.*,[21] and Stramska and Dickey.[22]

Our data preprocessing procedure excludes the influences of longer waves caused by storms, earthquakes, or tides. For our selected sunny days and calm ocean conditions, smooth and long-period (45 s–24 h) gravity waves may also play a role in the

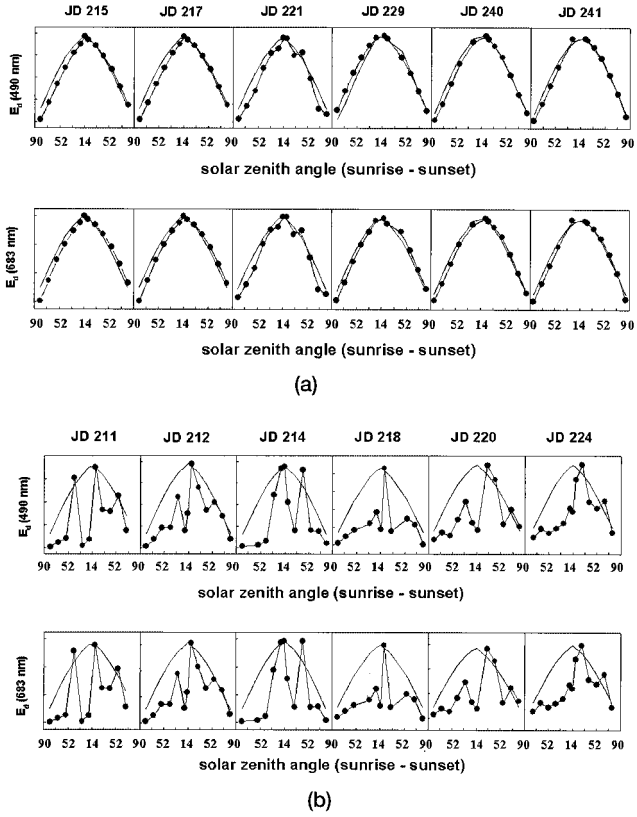

Fig. 3. (a) Daily profiles of E_d for six good Julian days, obtained under favorable sky, surface, and water body conditions. The upper and lower rows of subplots correspond to E_d at 490 and 683 nm, respectively. E_d is presented in relative units; therefore y-axis tick labels are omitted for clarity. The solid curve represents cos θ_a, normalized to the maximum of E_d in each day. (b) Daily profiles of E_d for six bad Julian days. The plotting configuration is similar to that in (a). JD, Julian days; they are labeled above the plots.

fluctuation of the underwater light field but cannot be assessed by the 45-s sampling period. We evaluated the effect of these longer waves by analyzing the variation of water pressure at 14-m water depth. Results indicate that their influences on radiometer measuring accuracy are negligible compared with the short-term wave-focusing effect (see Appendix A).

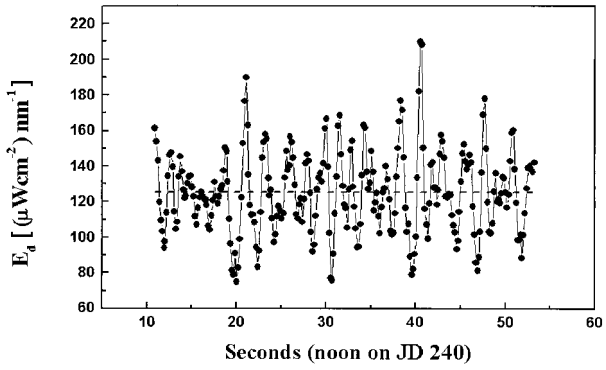

Fig. 4. E_d sampled at an interval of 45 s around local noon on Julian day 240 (JD 240), λ = 490 nm.

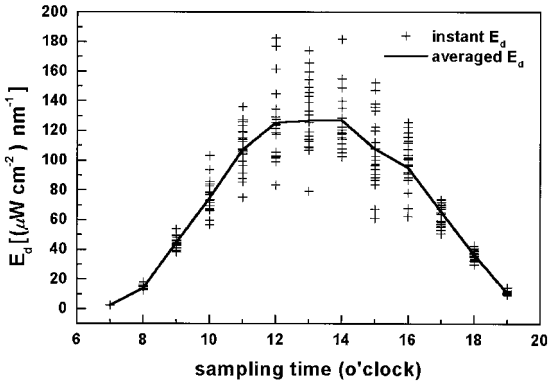

Fig. 5. Instantaneous and averaged E_d at 14-m water depth on Julian day 240, λ = 490 nm.

B. K_d Computations

The average K_d (in inverse meters) between 0^- and 14 m and between 14 and 21 m for the good data set was computed according to

$$K_d(0 \rightarrow 14 \text{ m}) = [\ln E_d(0^-) - \ln E_d(14 \text{ m})]/(14 - 0), \quad (2a)$$

$$K_d(14 \rightarrow 21 \text{ m}) = [\ln E_d(14) - \ln E_d(21 \text{ m})]/(21 - 14), \quad (2b)$$

where $E_d(0^-)$ is the time-averaged downwelling irradiance just below the water surface.

To calculate $E_d(0^-)$ from the measured downwelling irradiance just above the water surface [$E_d(0^+)$], we must have information about the spatial distribution of skylight and the air–water interface transmittances, which are functions of the solar zenith angle and atmospheric type. We use a simple model by Baker and Smith[23] to describe the downwelling irradiance just below the surface as a function of direct and diffuse reflections of light above and below the sea surface, air–sea interface transmittance, and wind speed. The total downwelling irradiance just above the air–water interface was decomposed into two components referred to as direct and diffuse irradiance or

$$E_d(0^+, \theta_a) = E_{\text{direct}}(0^+, \theta_a) + E_{\text{diffuse}}(0^+, \theta_a), \quad (3)$$

where θ_a is the solar zenith angle in air. The downwelling irradiance just below the surface is

$$E_d(0^-, \theta_w) = [1 - \rho_{\text{direct}}(\theta_a)]E_{\text{direct}}(0^+, \theta_a) + [1 - \rho_{\text{diffuse}}(\theta_a)]E_{\text{diffuse}}(0^+, \theta_a) + \rho_w E_u(0^-, \theta_w), \quad (4)$$

where ρ_{direct} and ρ_{diffuse} are the reflectances of direct solar and sky radiation, respectively, and ρ_w is the reflectance of diffuse radiation from below the air–sea interface. By introducing an irradiance reflectance, $R = E_u(0^-)/E_d(0^-)$, and a ratio of diffuse to total

downwelling irradiance, $y = E_{\text{diffuse}}/E_d$, we can rewrite Eq. (4) as

$$E_d(0^-, \theta_w) = \frac{1}{(1 - \rho_w R)} [(1 - \rho_{\text{direct}})(1 - y) + (1 - \rho_{\text{diffuse}})y] E_d(0^+, \theta_a) = \frac{1}{(1 - \rho_w R)} t(\theta_a) E_d(0^+, \theta_a), \quad (5)$$

where $t(\theta_a)$ is the global transmittance function and ρ_{direct} is computed with the Fresnel reflection law. Baker and Smith[23] found that ρ_w varies from 0.485 to 0.463 as a function of wind speed between 0 and 16 m s^{-1} and that R is 0.10 for clearest waters but typically varies between 0.02 and 0.10. We took $\rho_w = 0.47$ and $R = 0.10$ for our good days (sunny and low wind speed conditions). Uncertainties in ρ_w and R have negligible influence on the computations that use Eq. (5) in that $\rho_w R \ll 1$. By using the atmospheric transfer model of Tanre *et al.*[24] and accounting for the wind effect, Baker and Smith[23] computed values of the global transmittance, $t(\theta_a)$, in Eq. (5), spanning solar zenith angles from 0° to 85°, wavelengths from 300 to 700 nm, and visibility of 10–50 km for maritime and continental atmospheres. We performed a two-dimensional (wavelength and solar zenith angle) interpolation of the results obtained by Baker and Smith[23] and assumed a maritime atmospheric condition and a visibility of 30 km to obtain $t(\theta_a)$ at the seven wavelengths corresponding to our data and at various solar zenith angles. The reflectance from the direct radiation component was found to be relatively unaffected by wind, and the global transmittance changed by less than 1% for solar angles less than 70°. Therefore, to make our computation more reliable, we used data sets measured at zenith angles less than 70°. For BTM deployment #12, this corresponded to a sampling time period of approximately 8 a.m. to 4 p.m. Bermuda local time.

To separate elastic and inelastic components, we first decomposed E_d into two parts,

$$E_d = E_d^e + E_d^I, \quad (6)$$

where the superscript e represents the contribution of elastically scattered solar photons and the superscript I represents the contribution of light from inelastic scattering. The parameter η is introduced to represent the ratio of the inelastic scattering component to total E_d:

$$\eta = E_d^I/E_d. \quad (7)$$

Then total E_d can be rewritten as

$$E_d = E_d^e/(1 - \eta). \quad (8)$$

K_d is decomposed in a similar manner:

$$K_d = K_d^e - K_d^I. \quad (9)$$

The negative sign before K_d^I indicates that inelastic scattering causes decreases in K_d. By substituting Eq. (8) into Eqs. (2), we obtain

$$K_d^e(z_1 \to z_2; \theta_w) = \frac{1}{(z_2 - z_1)} \left[\ln \frac{E_d(z_1, \theta_w)}{E_d(z_2, \theta_w)} \right], \quad (10a)$$

$$K_d^I(z_1 \to z_2; \theta_w) = \frac{1}{(z_2 - z_1)} \left[\ln \frac{1 - \eta(z_1, \theta_w)}{1 - \eta(z_2, \theta_w)} \right]. \quad (10b)$$

In Eqs. (10a) and (10b) the two components of K_d are expressed explicitly as functions of depth and zenith angle. The wavelength dependence is implied.

C. Hydrolight Simulations

We employed a numerical model, Hydrolight 4.1, to investigate the influences of angular properties on inelastic scattering. Therefore our study differs from past studies of K_d variability in that we present model verification of our assumptions and hypotheses. Hydrolight solves radiative transfer equations in water on the basis of invariant imbedding theory.[25] Because the necessary IOPs required by Hydrolight were not collected at the test site during deployment #12 of the BTM project, we used a generic four-component IOP model[16] for case I waters.[25] It was assumed that the water body is composed of four constituents: pure seawater, chlorophyll, colored dissolved organic matter, and mineral particles. Waters off Bermuda are classified as case I waters; therefore an average chlorophyll-*a* concentration of 0.03 mg m^{-3}, as measured with a fluorometer moored at a 35-m depth during deployment #12,[19] was used for simulations. Sensitivity analyses show that simulated results are insensitive to chlorophyll concentrations below 0.1 mg m^{-3}. The colored dissolved organic material was assumed to covary with chlorophyll. The concentration of mineral particles was not measured and was taken to be zero because it plays a negligible role in the process of inelastic scattering. Sensitivity analyses show that minerogenic particles have a great influence on optical properties, particularly at the shorter wavelengths. However, Hydrolight results indicate that the concentration of minerogenic particles in the Sargasso Sea is less than 0.05 g m^{-3}. The wind speed at the sea surface was taken to be 4 m s^{-1}; the average wind speed measured during the 12 good days was 4.2 m s^{-1}. The model accounted for inelastic scattering sources including Raman scattering and chlorophyll fluorescence. A detailed formulation for incorporating inelastic scattering into the model can be found in Mobley.[25] Last, the ocean was assumed to be infinitely deep. The simulation was performed over a depth range of 0 to 98 m with a vertical grid spacing of 2 m.

3. Results and Discussion

The average diffuse attenuation coefficient, K_d, calculated from Eqs. (2) as a function of the solar zenith

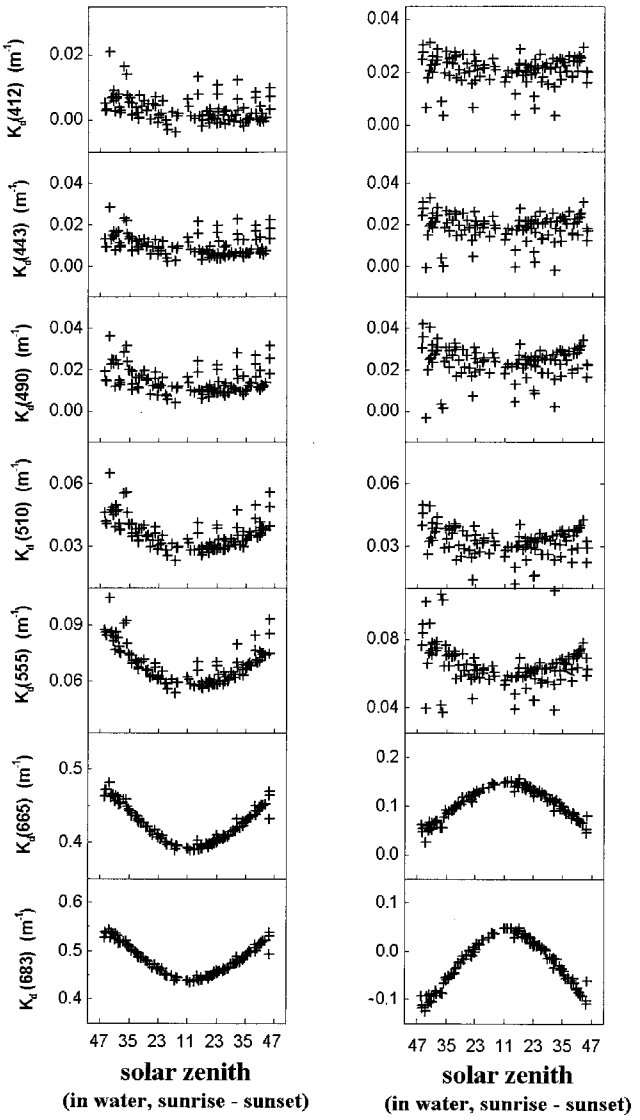

Fig. 6. $K_d(\lambda, \theta_w)$ in the upper (0 to 14 m; left panels) and deeper (14 to 21 m; right panels) layers, in units of inverse meters. The horizontal axes represent the refracted solar zenith angle, θ_w, in water, starting from sunrise at the left with sunset at the right; noon data are in the center.

angle is shown in Fig. 6 for all seven wavelengths within the upper (0- to 14-m) and deeper (14- to 21-m) layers for the good data. As mentioned previously, solar zenith angles at a certain sampling time varied in successive days, and therefore K_d is presented as a quasi-continuous function of the zenith angle. This is especially obvious at the two red wavelengths (665 and 683 nm), in which data points form smooth curves.

Although quasi-random uncertainties such as those caused by the wave-focusing effect are minimized during the data preprocessing procedure, residual fluctuations of the light field, which result in the scatter of data points especially at shorter wavelengths, are still apparent in the data sets (see Fig. 6). The negative values of K_d at 683 nm in the deeper layer are attributed to systematic measurement errors (e.g., biofouling and calibrations; see Appendix A). The presence of chlorophyll fluorescence may contribute to the negative values of K_d in the red wavelengths; however, chlorophyll fluorescence would not result in such large negative values. A quantitative evaluation of the possible errors associated with our data can be found in Appendix A.

K_d values show an increasing dependence on the zenith angle from the blue to the red wavelengths (Fig. 6). Principally, K_d represents the attenuation of irradiance and generally should be proportional to the path length of photons in water. For every 1 m of depth, the photons traverse a path length of $1/\mu$, where $\mu = \cos \theta_w$. An inverse relationship, or $K_d \propto 1/\mu$, is expected for a purely absorptive water body. However, in naturally occurring water bodies, scattering by water molecules and dissolved and suspended matter tends to cause the underwater light field to be more isotropic and less dependent on illumination geometry. The scattering intensity is inversely proportional to $\lambda^{-4.3}$ for molecular scattering[25] and to λ^{-1} for particle scattering.[26] Therefore K_d is less correlated with the incident zenith angle at the blue wavelengths than at the red wavelengths (Fig. 6). In addition, the relatively higher measurement uncertainties of K_d at the blue wavelengths make it even more difficult to observe an explicit correlation between K_d and the zenith angle.

In some areas of the world's oceans, the variability of K_d can be associated with IOP variability, attributed to tidal or diel processes or both. Supporting time-series measurements (chlorophyll concentration and beam attenuation coefficient at 660 nm; 3.75-min sampling rate) at 35-m water depth on Julian day 240 were analyzed to determine the dominant causes of variability in optical properties (data not shown). Results show that the chlorophyll concentration and the beam attenuation coefficient varied little with time, with the ratios of standard deviation/mean = 7% and 1.2%, respectively. In contrast, E_d on Julian day 240 varied by more than 2 orders of magnitude (Fig. 4). Therefore, although IOPs may have a small effect on optical variability in the Sargasso Sea, variations in E_d and K_d are primarily attributed to changes in solar radiation.

To better illustrate the influence of absorption, a, and scattering, b, on the $K_d - \theta_w$ relationship, we calculated correlation coefficients between measured K_d and $1/\mu$, as well as the ratio of b/a (Fig. 7). The values for absorption coefficient $a(\lambda)$ and scattering coefficient $b(\lambda)$ were computed by use of models by Morel[26] and a chlorophyll concentration of 0.03 mg m^{-3}. The chlorophyll concentration was inferred from *in situ* fluorometric measurements made at the 35-m depth on the BTM during deployment #12. As the wavelength increases from 412 to 683 nm, b/a decreases by 2 orders of magnitude (from 4.7 to 0.045) while the correlation coefficient of K_d and $1/\mu$ increases from ~0.2 to 0.9 (Fig. 7). Thus for higher b/a, K_d tends to be less dependent on the solar zenith angle owing to the relative increasing of scattering effects. In addition, the correlation between K_d and

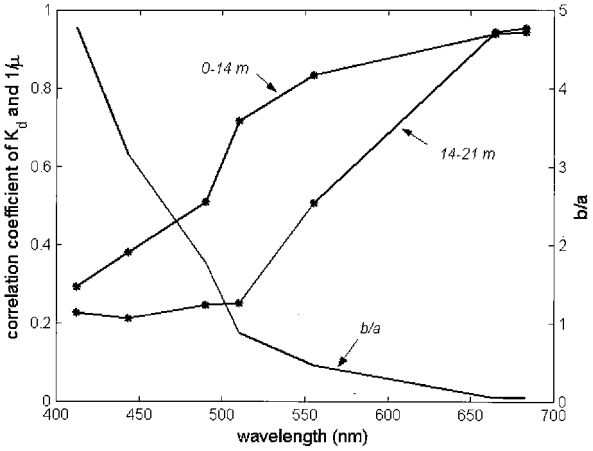

Fig. 7. Correlation of $K_d(\lambda)$ with $1/\mu$ and its dependence on b/a (curves with symbols). b/a is scaled on the right vertical axis (solid curve). K_d becomes less correlated with the refracted zenith angle for greater b/a values.

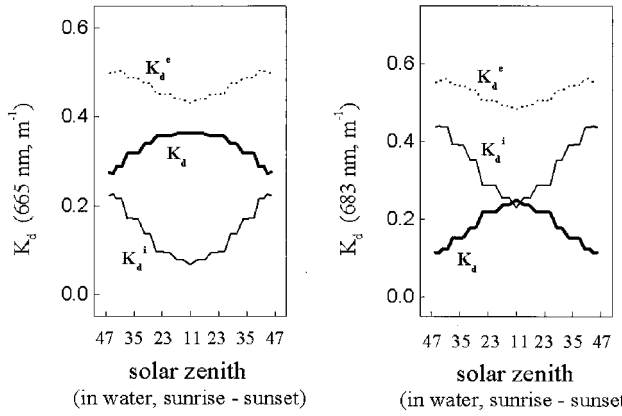

Fig. 8. Hydrolight-simulated K_d (in inverse meters) and its elastic and inelastic components in the deeper layer (14 to 21 m) at 665 and 683 nm. At larger θ_w, the inelastic component increases faster than the elastic component, which results in a smaller total K_d. The plotting configuration is similar to that in Fig. 6.

the solar zenith angle decreases with increasing depth because of a more isotropic light field at greater depth (Fig. 7). These results agree well with Kirk's prediction[27] by Monte Carlo simulations.

Angular dependencies of K_d at the five shorter wavelengths (412–555 nm) are similar within the upper and deeper layers (Fig. 6). However, a significant difference in K_d at the two red wavelengths (665 and 683 nm) is observed between the two layers. For example, at 683 nm, the values of K_d in the shallow layer decrease by 94% at noon and decrease in the deeper layer by 390% at sunrise and sunset. In addition, the angular patterns of K_d in the deeper layer are reversed from those in the upper layer and do not follow the $K_d \propto 1/\mu$ relationship. Numerical simulations[12,14] have shown that the decrease of K_d in the deeper layer at red wavelengths is caused by the existence of internal light sources, the most important of which are Raman scattering and chlorophyll fluorescence. Because the two internal light sources cannot be discriminated from each other by radiometric measurements, they are treated together as inelastic scattering. The basic condition for an explicit inelastic scattering effect is a significant difference of attenuation rates between excitation and emission photons. Although photons of red wavelengths attenuate rapidly with depth owing to significant absorption, inelastically scattered photons from shorter wavelengths attenuate at a much slower rate. Therefore the relative contribution of inelastic scattering to E_d increases with depth and results in a decreasing attenuation rate of E_d. Although inelastic scattering exists over the entire visible spectrum, no significant inelastic scattering effect is observed at the five shorter wavelengths (412–555 nm) because the attenuation coefficients for excitation and emission photons are similar within this spectral band. For K_d at 665 and 683 nm, the opposite angular pattern between the two layers (Fig. 6) implies that the number of inelastic photons increases rapidly with the zenith angle and that the increase is faster than the loss of direct solar photons because of a longer path length at a greater zenith angle. Consequently, a larger inelastic scattering contribution to E_d and decreased K_d values for larger zenith angles are observed.

To study the influences of angular properties on inelastic scattering, we included or excluded inelastic scattering in Hydrolight simulations performed at 665 and 683 nm with $z_1 = 14$ m and $z_2 = 21$ m. The inelastic component K_d^I increases much faster with zenith angle than the elastic component K_d^e does, which results in a decrease of K_d at a larger zenith angle according to Eq. (9) (Fig. 8). The step pattern of the simulated curves (Fig. 8) was caused by a default zenith angle interval of 10° for reasonable computation efficiency. Because the simulation results in this study were used as a tool for a better understanding of angular patterns rather than a verification of absolute values, we did not modify the Hydrolight code to obtain results for higher angular resolution.

The dependence of K_d on depth is also significantly influenced by inelastic scattering. Figure 9(a) shows the simulated $\eta(z)$ at seven wavelengths within a depth range of 0 to 90 m. For the four shorter wavelengths (412–510 nm), η is approximately zero and almost invariant with depth, indicating a negligible inelastic scattering effect on E_d. At depths greater than 60 m, the inelastic component at 555 nm increases. Considerable variation in η is observed at the two red wavelengths (665 and 683 nm). η increases rapidly from nearly zero to almost 1 within the upper ~25 m. This results in a rapid increase in the inelastic component K_d^I and a significant decrease in K_d, as shown in Fig. 9(b).

For our data set, we suggest a natural division of the water column into three distinct layers according to the characteristic patterns of $\eta(z)$ in each layer. This is generally consistent with the characterization by Stramska and Frye[7] and Berwald *et al.*[14]

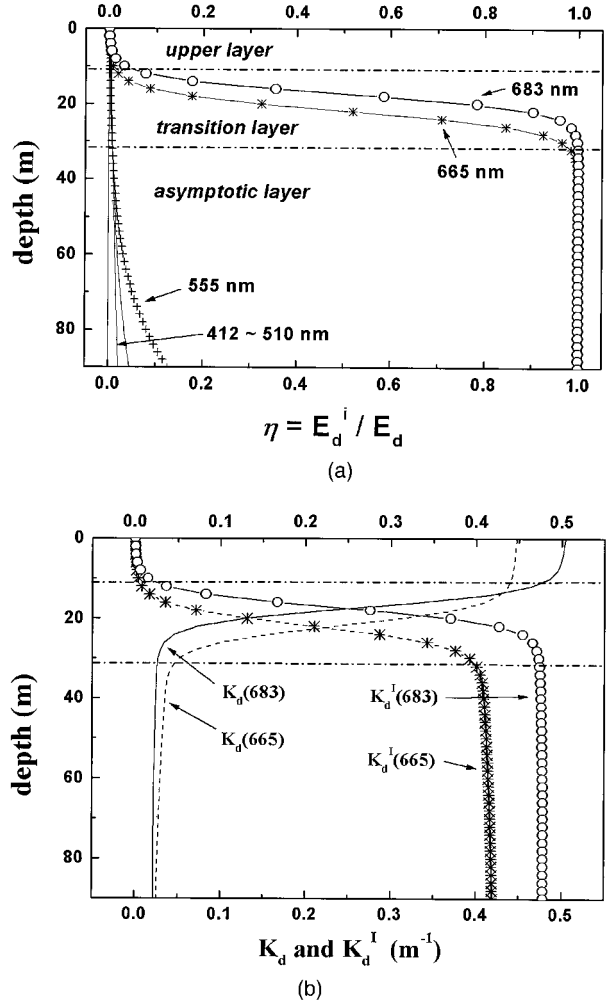

Fig. 9. (a) Ratio of the inelastic component to total E_d, $\eta(z)$, at seven wavelengths. The water column is partitioned into three layers for 665 and 683 nm. (b) The total K_d and its inelastic component K_d^I in the suggested three layers of the Sargasso Sea.

(i) The upper layer, in which $\eta(z) \approx 0$; inelastic scattering has a negligible influence on K_d, i.e., $K_d^I \approx 0$; and K_d is almost solely determined by absorption and elastic scattering. The depth range of this layer in our case is approximately 0 to 12 m.

(ii) The transition layer, in which $0 < \eta(z) < 1$ and $\eta(z)$ increases rapidly with depth. The most significant inelastic scattering effect is observed in this layer. The depth range for the transition layer is approximately 12 to 35 m for the Sargasso Sea. The characteristics of the transition layer are derived from the large differences between the attenuation rates of the excitation and emission radiation.

(iii) The asymptotic layer, in which $\eta(z)$ is nearly constant and approximately equal to 1. Preisendorfer[28] first described the existence of the asymptotic field, and later Højerslev and Zaneveld[29] presented a rigorous mathematical proof. Also, Berwald *et al.*[14] have more recently discussed this region in detail. The properties of the light field in this layer are almost completely determined by IOPs; i.e., K_d is independent of depth or zenith angle. Although inelastic scattering is dominant in this layer, it actually has no influence on the angular or depth dependence of K_d. K_d values are constant within this layer.

Note that this layered pattern is not a definition of a water-column property but rather a characteristic of inelastic scattering on K_d at the red wavelengths. Also, this partitioning of the water column and the corresponding depth ranges are valid only for the Sargasso Sea for wavelengths >550 nm, where inelastic scattering plays a significant and even determinative role in characterizing the light field at greater depths. The suggested three-layer structure will be less obvious for wavelengths >700 nm owing to the strong absorption at the near-infrared region, although inelastic scattering still exists. For shorter wavelengths, although K_d is not constant and varies with depth even in a homogeneous water body, its rate of change with depth is much smaller than that of red wavelengths and no large gradient is observed. The division of the three layers is by no means absolute; it is dependent on wavelengths, constituents of the water column, and the solar zenith angle. Berwald *et al.*[14] have presented a detailed analysis based on numerical modeling of Raman-scattering effects on K_d as a function of depth.

To compare the behavior of K_d under differing environmental conditions, we performed similar analyses for data sampled during bad days (overcast skies and rough sea surface) (Fig. 10). A weak dependence of K_d on the zenith angle is apparent at all wavelengths and in both layers for overcast conditions, which is expected in that there is no predominant direction in the downwelling light field without direct solar illumination. For the two red wavelengths (665 and 683 nm), K_d in the deeper layer is approximately one half to one third of that in the upper layer, indicating a significant inelastic scattering effect similar to the good data.

The spectral patterns of K_d in the upper layer and deeper layer are shown in Fig. 11. In the deeper layer, $K_d(\lambda)$ values decrease at the red wavelengths owing to the relative increase of inelastic photons. In addition, inelastic scattering weakens the spectral dependence of $K_d(\lambda)$ and flattens the $K_d(\lambda)$ spectrum at greater depths. Variations in the solar zenith angle and the sky condition do not have a significant influence on the spectral properties of $K_d(\lambda)$.

4. Summary

High-resolution time-series observations of downwelling irradiance from the Bermuda Testbed Mooring program facilitate a time–space transformation of discrete temporal samplings into a quasi-continuously distributed data set over a broad range of zenith angles. Averaged diffuse attenuation coefficients of downwelling irradiance (K_d) were calculated at seven wavelengths in the visible. We focused on the variation of K_d and its elastic and inelastic components as related to the solar zenith angle. The dependencies of K_d on sky and wind

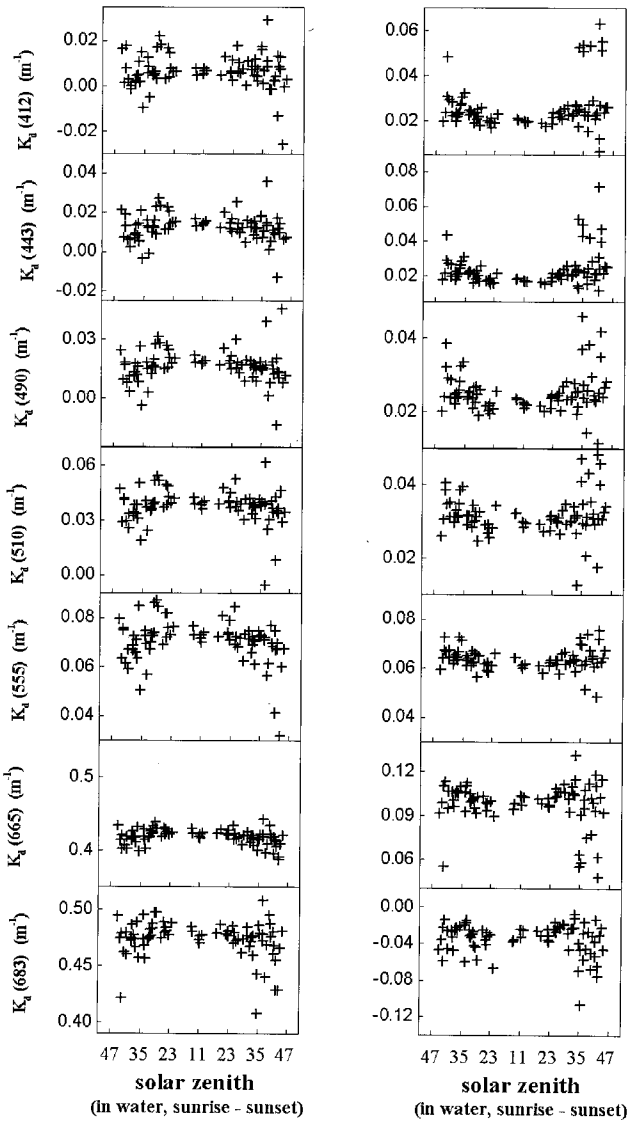

Fig. 10. $K_d(\lambda, \theta_w)$ under overcast conditions. The plotting configuration is the same as that in Fig. 6.

(wave) conditions, depth, and wavelength are also investigated. Our study improves upon past studies by including both observations and numerical simulations (Hydrolight) to test and verify assumptions and hypotheses.

K_d shows an increasing dependence on the solar zenith angle with wavelengths in both the upper (0- to 14-m) and deeper (14- to 21-m) layers. At shorter wavelengths (<510 nm), K_d has only a weak dependence on the solar zenith angle owing to the prevalence of the scattering effect over absorption processes. This effect tends to cause the underwater light field to be more isotropic. Therefore K_d at shorter wavelengths can be considered as a quasi-IOP. However, in absorption-dominated waters, e.g., at wavelengths >510 nm and in case I waters, K_d can be strongly dependent on the solar zenith angle and should be considered an apparent optical property.

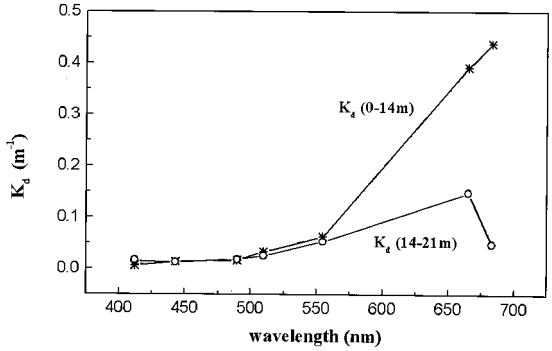

Fig. 11. $K_d(\lambda)$ of two layers under sunny sky and with a zenith angle of 14°. K_d decreases at the red wavelengths and flattens at the deeper depth; both effects are due to the inelastic scattering.

Inelastic scattering plays a significant role in characterizing the underwater light field at red wavelengths (e.g., 665 and 683 nm) and at increasing depths. K_d greatly decreases at large zenith angles (Fig. 6) and K_d spectra flatten (Fig. 11) at deeper depths because of inelastic scattering. Owing to the large difference of attenuation rate between excitation and emission photons of inelastic scattering, a large gradient in K_d with depth is observed at red wavelengths [Fig. 9(b)]. We suggest that at red wavelengths (>600 nm) the water column may be divided into three layers for Sargasso Sea waters: upper, transition, and asymptotic layers, according to the strength of influence of inelastic scattering. This is consistent with the theoretical results of Berwald *et al.*[14] and experimental results of Stramska and Frye.[7] K_d is independent of inelastic scattering in the upper layer and most significantly influenced by inelastic scattering in the transition layer. In the asymptotic layer, K_d can be characterized as an IOP.

The results from this direct and comprehensive examination of the angular properties of K_d in case I seawater, accounting for the inelastic scattering effects at the red portion of the visible spectrum can be used to improve the characterization of the underwater light field. Higher-accuracy measurements will be carried out in future research for more quantitative studies of apparent optical properties.

Appendix A: Error Analysis

We investigate four sources contributing to the radiometer measurement error: drifting clouds, buoy shadowing, wave effect (short-term and long-period), and radiometer uncertainty. Our data preprocessing procedure, in which the correlation between solar irradiance and the cosine of the solar zenith is calculated as a threshold for selecting sunny days, excludes the days with drifting clouds or storm weather. Therefore we assume that the cloud effect is negligible in our data sets in good days.

The BTM buoy has a diameter of 2.5 m and subtends a half-angle of 5.1° and 3.4° in water to E_d radiometers at 14- and 21-m depths, respectively. The smallest in-water solar zenith angle in the selected 12 good days is 10.5°. Thus the buoy will

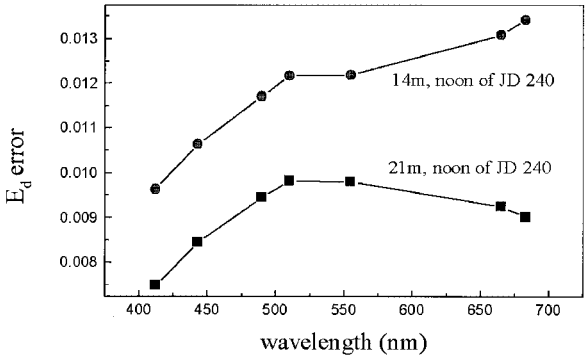

Fig. 12. Average spectral error in E_d that is due to short-term wave focusing and defocusing.

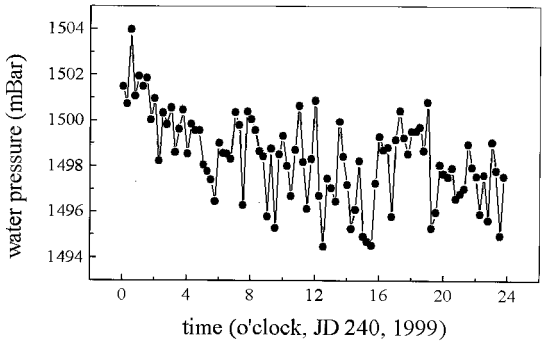

Fig. 13. Daily time series of water pressure measured at 14 m on Julian day 240.

never shade the directly diffracted solar beam for our case. According to a simulation made by Gordon, the error that is due to shadowing will be virtually independent of scattering when $aR \ll 1$, where a is the absorption coefficient of seawater and R is the radius of a shadowing object, i.e., the buoy in our case. Under this circumstance, the error is primarily attributed to the shadowing of a direct solar beam. The absorption coefficient, a, can be easily calculated with the model by Morel,[26] assuming a chlorophyll concentration of 0.03 mg m^{-3}. For shorter wavelengths (412–555 nm), a is 0.013–0.064 m^{-1} and aR is 0.016–0.08. For the two red wavelengths (665 and 683 nm), a is 0.43–0.49 m^{-1} and aR is 0.54–0.61. At depths of 14 and 21 m, there are actually few direct photons at the two red wavelengths because of strong absorption [see Fig. 9(a)], and almost all red photons come from inelastic scattering. Therefore, although aR is close to 1.0 at the red wavelengths, the shadowing error is negligible, as it is at shorter wavelengths. We conclude that the overall error of buoy shadowing is negligible for our measured data sets.

Figure 4 shows that wave focusing and defocusing will generate short-term variations of downwelling irradiance. On the basis of a conventional approach,[30] we take the relative standard deviation of the mean of the downwelling irradiance [or $\sigma/(m\sqrt{n})$, where σ is the standard deviation, m is the mean, and n is the number of samples within the 45-s sampling period] as the E_d error that is due to short-period waves. Figure 12 shows this E_d error at 14 and 21 m, at noon of Julian day 240. In addition to the correlation with wind speed, the curve has an obvious dependence on wavelength. Stramska and Dickey[22] gave a detailed discussion on the spectral properties of light fluctuation. According to Fig. 12, we take 1% as a rough estimate of E_d errors that are due to short-term light fluctuation.

Smooth and long-period (>45 s) waves might not be detected within the 45-s sampling period and still play a role in the fluctuation of the underwater light field. Because the light path length over the radiometer is proportional to the water pressure, we can estimate the influence of longer waves by measuring the variation of water pressure. Figure 13 shows the water pressure measured at 14 m on Julian day 240 with a sampling interval of 37.5 s. A simple calculation shows that $\sigma/(m\sqrt{n})$ is approximately 1.3×10^{-5} within 24 h. Therefore errors in E_d that are due to long-period waves are negligible compared with those that are due to short-term wave focusing and defocusing in the selected good days and calm ocean surfaces.

Another important error source is the uncertainty of the irradiance radiometer, which might be induced by calibration, optical and mechanical adjustment, and electronic processing. The radiometers are inspected and calibrated by the manufacturer before and after each deployment. An overall error of approximately 3% for our OCI-200 irradiance radiometer is assumed.[31]

The two main sources of error for underwater irradiance are short-term wave effect and radiometer uncertainties. Their combined error is approximately 3.2% {square root of $[(1\%)^2 + (3\%)^2]$}. Note that measurement errors are a function of wavelength and depth.

To evaluate the error of K_d on the basis of the error of E_d, we need to use the propagation law of uncertainty.[30] Supposing that the uncertainties in downwelling irradiances at two depths, $E_d(z_1)$ and $E_d(z_2)$, are defined as u_1 and u_2, respectively. According to the definition of K_d in Eqs. (2), the uncertainty of K_d is expressed as

$$u_{K_d}^2 = \left[\frac{\partial K_d}{\partial E_d(z_1)}\right]^2 u_1^2 + \left[\frac{\partial K_d}{\partial E_d(z_2)}\right]^2 u_2^2 = \left(\frac{1}{z_2 - z_1}\right)^2 \left[\frac{u_1}{E_d(z_1)}\right]^2 + \left(\frac{1}{z_2 - z_1}\right)^2 \left[\frac{u_2}{E_d(z_2)}\right]^2. \quad \text{(A1)}$$

To simplify, we neglect the uncertainties of z_1 and z_2. Taking 3.2% as overall measuring error of E_d, i.e., $u_1/E_d(z_1) = u_2/E_d(z_2) = 3\%$, we calculate the uncertainty of K_d for the upper layer (0 to 14 m) by using Eq. (A1) to be $u_{K_d} = 0.003$ m^{-1} and for the deeper layer (14 to 21 m) by using $u_{K_d} = 0.006$ m^{-1}. At shorter wavelengths (412–490 nm), the value of K_d is approximately 0.02 m^{-1}, thus $u_{K_d}/K_d = 15\%$–30%; i.e., the errors of E_d will result in errors of K_d as large

as 15% to 30% for shorter wavelengths. However, for red wavelengths such as 665 and 683 nm, the values of K_d are as large as approximately 0.5 m^{-1} and, correspondingly, $u_{K_d}/K_d = 0.6\%–1.2\%$. This explains the lower scatter in measured K_d values at longer wavelengths compared with those at shorter wavelengths (Fig. 6). Generally, the errors in our measured data are within 30% (20% on average) depending on wavelength and depth.

In Fig. 6, negative K_d is observed at 683 nm in the deeper layer (14–21 m). This seems to imply an increase of downwelling flux with depth, which conflicts with the law of energy conservation. However, the $K_d \sim$ zenith curve looks smooth despite the abnormal K_d values, which indicates a significant systematic error embedded in 683-nm data (Fig. 6). According to the calibration reports of the irradiance radiometers, the calibration coefficients of the 683-nm channel at 21 m decreased by nearly 100% before and after deployment #12. It is most likely that this particular radiometer overestimated the downwelling irradiances at 683 nm and resulted in an abnormally small K_d in the deeper layer. The reason for the change in the calibration coefficient is still under discussion, and we suspect biofouling contributed primarily to this variability.

A simple analysis shows that these systematic errors do not influence the dependencies of K_d on the zenith angle, wavelength, or depth, which are the foci of this manuscript. Any systematic error can be expressed as a multiplicative factor of the true value. Supposing ϵ_1 and ϵ_2 are the error factors of downwelling irradiance, E_d, at z_1 and z_2, respectively, then

$$\begin{aligned} K_d &= \frac{\ln \epsilon_1 E_d^{\,0}(z_1) - \ln \epsilon_2 E_d^{\,0}(z_2)}{z_2 - z_1} \\ &= \frac{\ln E_d^{\,0}(z_1) - \ln E_d^{\,0}(z_2)}{z_2 - z_1} + \frac{\ln(\epsilon_1/\epsilon_2)}{z_2 - z_1} \\ &= K_d^{\,0} + \epsilon, \end{aligned} \tag{A2}$$

where the superscript 0 represents the true value. From Eq. (A2), the multiplicative error factors of E_d were transformed into additive terms, ϵ (added to the true $K_d^{\,0}$). Because systematic error is independent of external factors such as zenith angle, depth, etc., ϵ generates only a constant background signal and will not influence the relationships between K_d and these factors. This is consistent with 683-nm data shown in Fig. 6.

We thank Sarah Zedler and Songnian Jiang for help with data preparation and processing and Derek Manov, Frank Spada, and Xuri Yu for their valuable contributions. Support for this research was provided by the National Science Foundation Ocean Technology and Interdisciplinary Coordination and Chemical Oceanography Programs (TD: OCE-9627281, OCE-9730471), National Aeronautics and Space Administration (TD: NAGW-3949, NAS5-97127), the Office of Naval Research, the National Ocean Partnership Program, and the University of California, Santa Barbara.

References

1. N. G. Jerlov, *Marine Optics* (Elsevier, Amsterdam, 1976).
2. N. K. Hojerslev, "Daylight measurements for photosynthetic studies in the Western Mediterranean," Univ. Copenhagen Inst. Phys. Oceanogr. Rep. 26 (Univ. of Copenhagen, Copenhagen, 1974).
3. J. H. Nielsen and E. Aas, "Relation between solar elevation and the vertical attenuation coefficient of irradiance in Oslofjorden," Univ. of Oslo Rep. 31 (Univ. of Oslo, Oslo, 1977).
4. K. S. Baker and R. C. Smith, "Quasi-inherent characteristics of the diffuse attenuation coefficient for irradiance," in *Ocean Optics VI*, S. Q. Duntley, ed., Proc. SPIE **208,** 60–63 (1979).
5. H. R. Gordon, "Monte Carlo simulations for interpretation of irradiance measurements from moored instruments: preliminary results," in *Ocean Optics XI*, G. D. Gilbert, ed., Proc. SPIE **1750,** 366–370 (1992).
6. W. H. Wilson, "Spreading of light beams in ocean water," in *Ocean Optics VI*, S. Q. Duntley, ed., Proc. SPIE **208,** 64–72 (1979).
7. M. Stramska and D. Frye, "Dependence of apparent optical properties on solar altitude: experimental results based on mooring data collected in the Sargasso Sea," J. Geophys. Res. **102,** 15679–15691 (1997).
8. H. R. Gordon, "Can the Lambert–Beer law be applied to the diffuse attenuation coefficient of ocean water?" Limnol. Oceanogr. **34,** 1389–1409 (1989).
9. J. T. O. Kirk, "Volume scattering function, average cosine, and the underwater light field," Limnol. Oceangr. **36,** 455–467 (1991).
10. S. Sugihara, M. Kishino, and N. Okami, "Contribution of Raman scattering to upward irradiance in the sea," J. Oceanogr. Soc. Jpn. **40,** 397–404 (1984).
11. R. H. Stavn, "Raman-scattering effects at the shorter visible wavelengths in clear ocean waters," in *Ocean Optics X*, R. W. Spinrad, ed., Proc. SPIE **1302,** 94–100 (1990).
12. R. H. Stavn, "Effects of Raman scattering across the visible spectrum in clear water: a Monte Carlo study," Appl. Opt. **32,** 6853–6863 (1993).
13. R. H. Stavn and A. D. Weidemann, "Raman scattering in ocean optics: quantitative assessment of internal radiant emission," Appl. Opt. **31,** 1294–1303 (1992).
14. J. Berwald, D. Stramski, C. Mobley, and D. Kiefer, "Effects of Raman scattering on the average cosine and diffuse attenuation coefficient of irradiance in the ocean," Limnol. Oceanogr. **43,** 564–576 (1998).
15. D. Siegel and T. Dickey, "Characterization of downwelling spectral irradiance fluctuations," in *Ocean Optics IX*, M. A. Blizard, ed., Proc. SPIE **925,** 67–74 (1988).
16. C. Mobley and L. Sundman, *Hydrolight 4.1 Technical Documentation* (Sequoia Scientific, Inc., Redmond, Wash., 2000).
17. T. Dickey, D. Frye, H. Jannasch, E. Boyle, D. Manov, D. Sigurdson, J. McNeil, M. Stramska, A. Michaels, N. Nelson, D. Siegel, G. Chang, J. Wu, and A. Knap, "Initial results from the Bermuda Testbed Mooring Program," Deep-Sea Res. I **45,** 771–794 (1998).
18. T. Dickey, S. Zedler, D. Frye, H. Jannasch, D. Manov, D. Sigurdson, J. McNeil, L. Dobeck, X. Yu, T. Gilboy, C. Bravo, S. C. Doney, D. A. Siegel, and N. Nelson, "Physical and biogeochemical variability from hours to years at the Bermuda Testbed Mooring site: June 1994–March 1998," Deep-Sea Res. II **48,** 2105–2140 (2001).
19. S. Zedler, X. Yu, S. Jiang, T. D. Dickey, D. Manov, D. Sigurdson, and F. Spada, *Bermuda Testbed Mooring Data Report for*

Deployment #12 (Ocean Physics Laboratory, Univ. of California at Santa Barbara, Santa Barbara, Calif., 1999).
20. J. T. O. Kirk, *Light and Photosynthesis in Aquatic Ecosystems*, 2nd ed. (Cambridge U. Press, Cambridge, UK, 1994).
21. J. Zaneveld, E. Boss, and A. Barnard, "Influence of surface waves on measured and modeled irradiance profiles," Appl. Opt. **40,** 1442–1449 (2001).
22. M. Stramska and T. Dickey, "Short-term variability of the underwater light field in the oligotrophic ocean in response to surface waves and clouds," Deep-Sea Res. I **45,** 771–794 (1998).
23. K. S. Baker and R. C. Smith, "Irradiance transmittance through the air/water interface," in *Ocean Optics X*, R. W. Spinrad, ed., Proc. SPIE **1302,** 556–565 (1990).
24. D. Tanre, M. Herman, P. Y. Deschamps, and A. DeLeffe, "Atmospheric modeling for space measurements of ground reflectances, including bidirectional properties," Appl. Opt. **18,** 3587–3594 (1979).
25. C. D. Mobley, *Light and Water: Radiative Transfer in Natural Waters* (Academic, San Diego, Calif., 1994).
26. A. Morel, "Light and marine photosynthesis: a spectral model with geochemical and climatological implications," Prog. Oceanorgr. **26,** 263–306 (1991).
27. J. T. O. Kirk, "Dependence of relationship between inherent and apparent optical properties of water on solar altitude," Limnol. Oceanogr. **29,** 350–356 (1984).
28. R. W. Preisendorfer, "Theoretical proof of the existence of characteristic diffuse light in natural waters," J. Mar. Res. **18,** 1–9 (1959).
29. N. K. Hojerslev and J. R. V. Zaneveld, "A theoretical proof of the existence of the submarine asymptotic daylight field," Univ. Copenhagen Inst. Phys. Oceanogr. Rep. 34 (Univ. of Copenhagen, Copenhagen, 1977).
30. B. N. Taylor and C. E. Kuyatt, "Guidelines for evaluating and expressing the uncertainty of NIST measurement results," NIST Tech. Note 1297 (National Institute of Standards and Technology, Gaithersburg, Md., 1994).
31. M. Lewis, Dalhousie University, Halifax, Nova Scotia B3H 4J1, Canada, and Satlantic, Inc., 3295 Barrington Street, Halifax, NS B3K 5X8, Canada (personal communication, 2001).